Proceedings of the 12th International and 52nd National Conference on Fluid Mechanics and Fluid Power (FMFP)
December 19-21, 2025, Nirma University, Gujarat, India

FMFP2025-MPF-214

Multiphase Euler–Euler modeling of Fluidized-Bed Flotation: Effect of KTGF and Drag Closure Models

Yash Rathod[1], Ashish Raman[1] and Gaurav Bhutani[1,*]

[1]School of Mechanical and Materials Engineering, Indian Institute of Technology Mandi, Himachal Pradesh 175075, India
* Corresponding Author, email:gaurav@iitmandi.ac.in

ABSTRACT This computational fluid dynamics (CFD) study investigates the hydrodynamics of a scaled, realistic fluidized-bed flotation (FBF) cell using the Euler–Euler model in OpenFOAM's `twoPhaseEulerFoam` solver. The simulations replicate a geometry for which companion experiments were previously conducted by our collaborators at the University of Queensland. Eleven model combinations, varying Kinetic Theory of Granular Flow (KTGF) and drag closures, were run in full 3-D. A grid-independence study established convergence at a 650k-cell mesh, yielding bed heights of 0.29–0.31 m in agreement with the experiments. Among the models tested, the Syamlal–O'Brien drag model (in conjunction with the Gidaspow viscosity model) produced the closest match to the measured bed height with an error of 6%. Axial and radial solids volume fraction profiles provided insights into flow patterns, critical for optimizing coarse particle recovery in mineral processing.

Keywords: Multiphase Flow Modeling, Fluidized Bed Flotation, OpenFOAM, KTGF, Drag Models

I. INTRODUCTION

Fluidized-bed flotation (FBF) has been recognized as a promising technique for recovering coarse mineral particles ($\gtrsim$ 150 μm) from low-grade ores, while offering lower energy consumption compared to conventional flotation systems [1]. Unlike conventional flotation, where particles must be ground to very fine sizes (<100 μm), coarse particle flotation reduces the extent of comminution required. Since grinding is the most energy-intensive stage of mineral processing, this shift translates into significant overall energy savings, in addition to improving coarse particle recovery [2]. By suspending particles in an upward liquid flow, FBF cells create a dynamic fluidized bed where particle–bubble interactions drive separation. In contrast to mechanically stirred tanks, where excessive turbulence can detach particles from bubbles, FBF systems naturally sustain an optimum turbulence regime—sufficient to keep coarse particles suspended and promote collisions, yet gentle enough to preserve stable bubble–particle attachments. This hydrodynamic balance enhances recovery efficiency and makes FBF particularly suitable for low-grade ores in copper, gold, and phosphate industries [3]. With increasing interest in the treatment of coarser feeds and the scale-up of new cell designs, reliable multiphase models are required to support geometry optimization and operational parameter selection [4].

Computational fluid dynamics (CFD) has been employed extensively to investigate liquid–solid transport in FBF cells [4]. Within the two-fluid (Euler–Euler) framework, both liquid and solid phases are represented as interpenetrating continua [5]. Solid-phase stresses are typically described through the Kinetic Theory of Granular Flow (KTGF) [6], while interphase momentum transfer is prescribed using drag correlations [7], [8]. Prior investigations have shown that the choice of these closure models strongly influences predictions of bed expansion and solids distribution; however, comprehensive evaluations of KTGF–drag model combinations in realistic FBF geometries have been limited [4], [9].

In the present work, the open-source solver `twoPhaseEulerFoam` in OpenFOAM has been used to simulate the hydrodynamics of a lab-scale FBF cell for which companion experimental measurements were provided by the Julius Kruttschnitt Mineral Research Centre (JKMRC), University of Queensland. Eleven model variations, spanning widely used drag laws and KTGF closures, have been examined. Model predictions have been validated against measured bed expansion, while axial and radial solids-volume-fraction distributions have been analyzed to quantify the sensitivities introduced by model choices.

This paper is organized as follows. Section II describes the governing equations, closure models, computational setup, and grid independence study. Section III presents the time evolution of bed heights and their validation with experimental data and the analysis of solids distributions for the model variants. Finally, Section IV summarizes the main conclusions and outlines directions for future work.

II. METHODOLOGY

A. Governing Equations

The Euler–Euler model was used to solve the continuity and momentum equations for the water and solid phases. For phase i (water or solid), the continuity equation is given as:

$$\frac{\partial(\alpha_i \rho_i)}{\partial t} + \nabla \cdot (\alpha_i \rho_i \boldsymbol{v}_i) = 0, \tag{1}$$

where α_i is the volume fraction, ρ_i is the density, and $\boldsymbol{v}_i$ is the velocity of phase i. The volume fractions satisfy the constraint:

$$\alpha_w + \alpha_s = 1. \tag{2}$$

The momentum equation incorporates the forces acting on each phase, including pressure, gravity, and interphase

interactions, and is given as:

$$\frac{\partial(\alpha_i \rho_i \boldsymbol{v}_i)}{\partial t} + \nabla \cdot (\alpha_i \rho_i \boldsymbol{v}_i \boldsymbol{v}_i) = -\alpha_i \nabla p + \alpha_i \rho_i \boldsymbol{g} + \nabla \cdot \bar{\bar{\tau}}_i + \boldsymbol{F}_i, \tag{3}$$

where p is the pressure, $\boldsymbol{g}$ is the gravitational acceleration, $\bar{\bar{\tau}}_i$ is the viscous stress tensor, and $\boldsymbol{F}_i$ accounts for interphase momentum exchange, primarily the drag force.

The viscous stress tensor $\bar{\bar{\tau}}_i$ is different for the two phases. For the water (liquid) phase it is modeled in Reynolds-averaged form with an effective viscosity $\mu_{\text{eff},w} = \mu_w + \mu_{t,w}$, where μ_w is the molecular viscosity and $\mu_{t,w}$ is the eddy viscosity obtained from the k–ε turbulence model. The stress tensor is expressed as:

$$\bar{\bar{\tau}}_w = 2\alpha_w \mu_{\text{eff},w} \bar{\bar{S}}_w + \alpha_w \left(-\frac{2}{3} \mu_{\text{eff},w} (\nabla \cdot \boldsymbol{v}_w) \right) \bar{\bar{I}}, \tag{4}$$

where $\bar{\bar{S}}_i$ is the rate of strain tensor, and $\bar{\bar{I}}$ is the identity tensor. The rate of strain tensor is defined as:

$$\bar{\bar{S}}_i = \frac{1}{2} \left(\nabla \boldsymbol{v}_i + (\nabla \boldsymbol{v}_i)^{\mathrm{T}} \right). \tag{5}$$

The standard k–ε model of Launder and Spalding [10] was used to determine $\mu_{t,w}$, with transport equations for turbulent kinetic energy k and dissipation ε as given in [6].

For the solid phase, the stress tensor is modeled using the KTGF [9]:

$$\bar{\bar{\tau}}_s = -p_s \bar{\bar{I}} + 2\alpha_s \mu_s \bar{\bar{S}}_s + \alpha_s \left(\lambda_s - \frac{2}{3} \mu_s \right) (\nabla \cdot \boldsymbol{v}_s) \bar{\bar{I}}, \tag{6}$$

where p_s is the solid granular pressure, μ_s is the shear viscosity, and λ_s is the granular bulk viscosity. The shear viscosity for solids is modeled as $\mu_s = \mu_{s,\text{kin}} + \mu_{s,\text{col}} + \mu_{s,\text{fr}}$, and the bulk viscosity λ_s follows the standard KTGF expression [9].

The solid granular pressure is modeled as a sum of kinetic and collisional contributions, given by:

$$p_s = \alpha_s \rho_s \Theta \left(1 + 2(1+e) g_0 \alpha_s \right), \tag{7}$$

where Θ is the granular temperature of solids, e is the restitution coefficient (taken as 0.9 in this work), and g_0 is the radial distribution function [9] given as $g_0 = \left[1 - (\alpha_s / \alpha_{s,\max})^{1/3} \right]^{-1}$.

The following granular temperature transport for Θ was solved:

$$\begin{aligned} \frac{3}{2} \Big[\partial_t (\alpha_s \rho_s \Theta) + \nabla \cdot (\alpha_s \rho_s \boldsymbol{v}_s \Theta) \Big] &= \bar{\bar{\tau}}_s : \nabla \boldsymbol{v}_s \\ &\quad + \nabla \cdot (\kappa_\Theta \nabla \Theta) \\ &\quad - \gamma_\Theta + \phi_{ws}, \end{aligned} \tag{8}$$

with the diffusion coefficient κ_Θ, collisional dissipation γ_Θ and the interphase energy exchange ϕ_{ws} as described in [6].

The interphase momentum exchange $\boldsymbol{F}_i$ includes the drag force only in this work:

$$\boldsymbol{F}_d = K_{cd} (\boldsymbol{v}_w - \boldsymbol{v}_s), \tag{9}$$

with K_{cd} depending on the choice of drag closure model—Syamlal–O'Brien [8], Gidaspow [7], etc. Lift, virtual mass and turbulent dispersion were neglected as in [6].

Table 1: **Boundary Conditions**

Property	Inlet	Walls	Outlet
Water			
Velocity (m/s)	0.30647	No slip	$\nabla \boldsymbol{v}_w \cdot \boldsymbol{n} = 0$
Sand			
Velocity (m/s)	0	No slip	$\nabla \boldsymbol{v}_s \cdot \boldsymbol{n} = 0$
Pressure	$\frac{\partial p}{\partial \boldsymbol{n}} = 0$	$\frac{\partial p}{\partial \boldsymbol{n}} = 0$	p_{atm}
Volume Fraction	$\alpha_s = 0$	$\nabla \alpha_s \cdot \boldsymbol{n} = 0$	$\nabla \alpha_s \cdot \boldsymbol{n} = 0$

Boundary conditions are listed in Table 1. No-slip walls, fixed inlet velocity, and atmospheric outlet pressure were applied. In addition, appropriate boundary conditions were specified for the granular temperature and turbulence quantities. For the granular temperature Θ, a zero-gradient condition was imposed at the inlet and outlet, while a partial slip condition was applied at the walls following Johnson and Jackson-type formulations [6]. For the turbulence model, standard k–ε wall functions were employed at the solid boundaries, with fixed inlet values of k and ε estimated from turbulence intensity and length scale correlations, and zero-gradient conditions at the outlet. These choices are consistent with common practice in multiphase RANS simulations.

B. Closure Models

Table 2: **Simulation cases with drag and KTGF closure variations. Case 1 is the base case.**

Case	Model Variation
1	Gidaspow Drag, Gidaspow Viscosity (Base Case)
2	Ergun Drag
3	Gibilaro Drag
4	Syamlal Viscosity
5	Syamlal Conductivity
6	Carnahan–Starling Radial Distribution
7	Syamlal–O'Brien Drag
8	Gidaspow–Schiller Drag
9	Gidaspow–Schiller (Modified)
10	Johnson–Jackson Frictional Stress
11	Syamlal–Rogers Pressure

The choice of interphase drag law and KTGF-based constitutive closures plays a central role in predicting liquid–solid fluidization behavior. To systematically assess their impact, eleven test cases were designed as listed in Table 2. Case 1 served as the *base case*, employing the commonly used Gidaspow drag law [7] along with the corresponding Gidaspow formulation for granular viscosity. All other cases represent one-at-a-time variations on this baseline, isolating the effect of a single closure modification.

The drag models examined included Ergun, Gibilaro, Syamlal–O'Brien [8], and Gidaspow–Schiller (standard and modified), in addition to the Gidaspow baseline. Variations in the KTGF closures included alternative formulations for granular viscosity (Syamlal), solid conductivity (Syamlal), radial distribution function (Carnahan–Starling), frictional stress (Johnson–Jackson [11]), and solids pressure (Syamlal–Rogers). This structured approach allows direct attribution

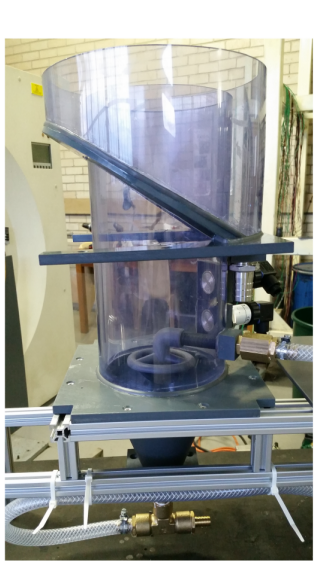

(a) **Experimental setup (JKMRC)**

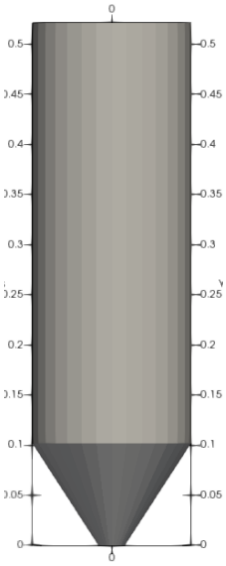

(b) **Numerical geometry; z-axis upwards**

Figure 1: **Experimental fluidized-bed flotation apparatus and corresponding numerical geometry of the conical-bottom cylindrical column.**

of observed changes in fluidization dynamics to individual model assumptions.

C. Discretization

The governing equations were discretized using the finite volume method (FVM) in OpenFOAM's `twoPhaseEulerFoam` solver. For a generic scalar field ϕ, the discretized transport equation is:

$$\frac{\phi_P^{n+1} - \phi_P^n}{\Delta t} V_P + \sum_f \left(\boldsymbol{v}_f \cdot \boldsymbol{A}_f\right) \phi_f = \sum_f D_f (\nabla \phi)_f \cdot \boldsymbol{A}_f + S_P, \tag{10}$$

where ϕ_P is the cell-center value, V_P is the cell volume, $\boldsymbol{A}_f$ is the face area vector, D_f is the diffusion coefficient, S_P is the source term, and n denotes the time step.

Convective terms used a second-order upwind scheme, which for the convection of a scalar ϕ is given as:

$$\phi_f = \phi_{\mathrm{U}} + \frac{1}{2} \left(\phi_{\mathrm{U}} - \phi_{\mathrm{UU}}\right), \tag{11}$$

where ϕ_f is the face-interpolated value. Temporal discretization employed a first-order implicit Euler scheme given by:

$$\frac{\phi_P^{n+1} - \phi_P^n}{\Delta t} = R(\phi^{n+1}), \tag{12}$$

where $R(\phi^{n+1})$ represents the discretized spatial and source terms. Timesteps were controlled to maintain Courant number Co$\leq$0.5. Diffusion terms used central differencing, and the PISO algorithm handled the pressure–velocity coupling.

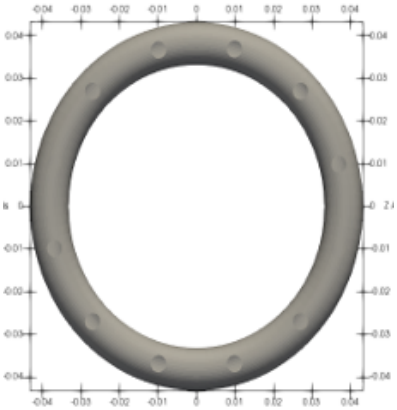

Figure 2: **Ring sparger with 12 holes (4 mm each) used at the column base; sparger in x–y plane.**

D. Simulation Setup

The fluidized-bed flotation cell was modeled as a conical-bottom cylindrical column (diameter 0.15 m, height 0.65 m) with a 12-hole sparger (hole diameter 4 mm each) [2]. The geometry was created in Blender and is similar to that used in [9], [6], which corresponded to the two-phase scaled fluidized-bed experiments performed at the JKMRC, Sustainable Minerals Institute (SMI) at University of Queensland [2]. The experimental apparatus and the corresponding numerical geometry are shown in Fig. 1, while the ring sparger is shown separately in Fig. 2. To prevent clogging of the sparger holes by solids, the sparger was oriented downwards in the experiments, and the same configuration was adopted in the simulations. Sand (ρ_s = 2650 kg/m^3, d = 250 μm, α_s = 0.6) formed a 0.16 m packed bed. Water was injected at a downward velocity of 0.31 m/s, corresponding to a superficial velocity of 2.5 mm/s. Simulations were run for 10 s of simulation time, which was sufficient for the case to reach steady state.

E. Grid Independence Study

Table 3: **Mesh Configurations**

Mesh	Grading (x, y, z)	Cells (blockMesh)	Cells (snappyHexMesh)
FM-2	(5,17,5)	425	20K
FM-1	(10,40,10)	4,000	200K
FM0	(15,60,15,2)	13,500	650K
FM1	(30,120,30)	108,000	1.2M
FM3	(60,204,60)	734,400	3.2M

Meshing used `blockMesh` and `snappyHexMesh` tools, with five configurations. Bed heights converged at 0.29–0.31 m for meshes $\geq$650K cells. Mesh configurations are detailed in Table 3. The FM0 mesh (650K cells) was selected, predicting a bed height of 0.30 m for the chosen case, matching experimental data. The bed expansion ratio for the different meshes at some initial time (non-steadystate) is compared in Fig. 3, which confirms that the solution becomes grid independent beyond FM0.

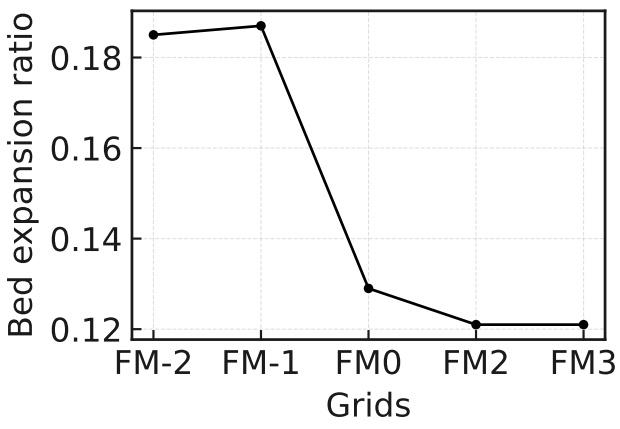

Figure 3: **Grid independence study showing bed expansion ratio across different mesh configurations.**

The FM0 mesh (650k cells) was found to offer a good balance between accuracy and cost, with further refinement (FM1 and FM3) increasing computational expense by factors of 4–10 while yielding negligible changes in bed height predictions (within 5%). A single 2 s simulation on FM0 typically required 6 hours on 48 cores, while FM3 required 5 days for comparable physical time.

F. Numerical Schemes

The `twoPhaseEulerFoam` solver was configured with solver tolerances set to 10^{-6} for pressure, velocity, and volume fraction fields to ensure convergence. Under-relaxation factors (0.3 for pressure, 0.7 for velocity) were applied to stabilize iterative solutions. The PISO algorithm, detailed in the discretization section, facilitated pressure–velocity coupling, with two corrector steps per iteration to enhance accuracy for multiphase flow dynamics.

III. RESULTS AND DISCUSSION

A. Flow Overview

To introduce the flow physics, instantaneous maps of the solids volume fraction α_s at representative times are shown in Fig. 4. These colormaps provide a qualitative view of bed expansion and interface evolution.

B. Parallel Scaling

Strong scaling tests were performed on the PARAM Himalaya cluster (Intel® Xeon® Gold 6248 @ 2.50 GHz) to quantify the reduction in wall time with increasing core counts. Runs were executed on *multiples of 12 cores* per node: 12, 24, and 48 cores on a single node, and then across 2, 3, and 4 nodes using all 48 cores per node. The reference case corresponds to 12 cores, and the speedup is reported as $S(N) = T_{12}/T_N$. Figure 5 shows that speedup is near-linear up to $N = 8 \times 12$ cores ($\approx 4.7\times$) and then tapers by $N = 12 \times 12$ cores ($\approx 5.1\times$), consistent with diminishing returns due to communication overheads and parallel efficiency limits for the chosen mesh size.

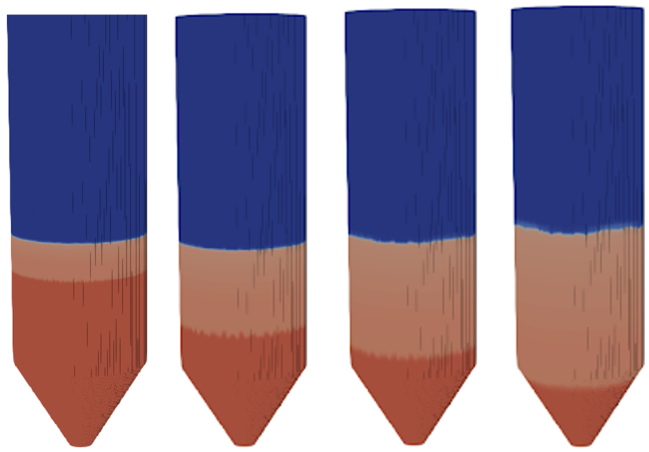

(a) t=**0.1 s** (b) t=**0.5 s** (c) t=**1 s** (d) t=**2 s**

Figure 4: **Instantaneous solids volume fraction α_s at four times showing bed expansion and interface evolution (common color scale across panels ranging between** 0 **and** 0.86**).**

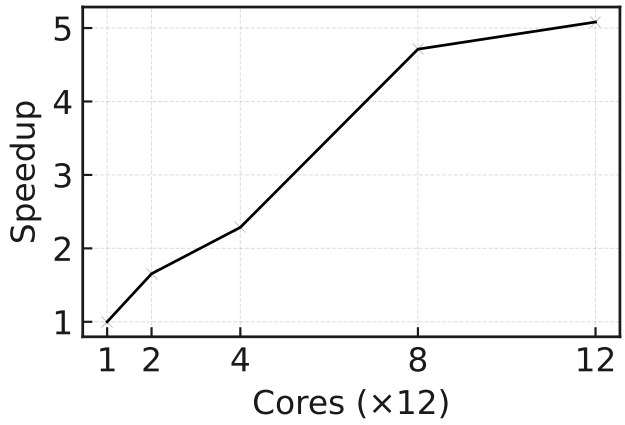

Figure 5: **Strong scaling of the solver on PARAM Himalaya showing speedup versus core count (in multiples of 12).**

C. Bed Height

Figure 6 shows the temporal evolution of the bed height $H(t)$ for Case 1. Starting from an initial packed height $H_0 = 0.16$ m, the bed rises rapidly in the first 2–3 s, then approaches a steady level of $H_\infty \approx 0.293$ m (the 95% settling time is $t_{95} \approx$ 6–7 s). The implied expansion ratio is $R_\infty = (H_\infty - H_0)/H_0 \approx 0.83$. A solids volume balance, $\alpha_{s,0} H_0 = \alpha_{s,\text{avg}} H_\infty$ with $\alpha_{s,0} = 0.60$, yields $\alpha_{s,\text{avg}} \approx 0.33$, consistent with the surface-averaged $\alpha_s(z)$ profiles reported later. The monotonic, non-oscillatory approach to H_∞ indicates that, under the Case 1 model, the interphase drag rapidly balances the submerged particle weight without triggering wave-like bed oscillation.

The steady expanded bed height H_∞ is compared with

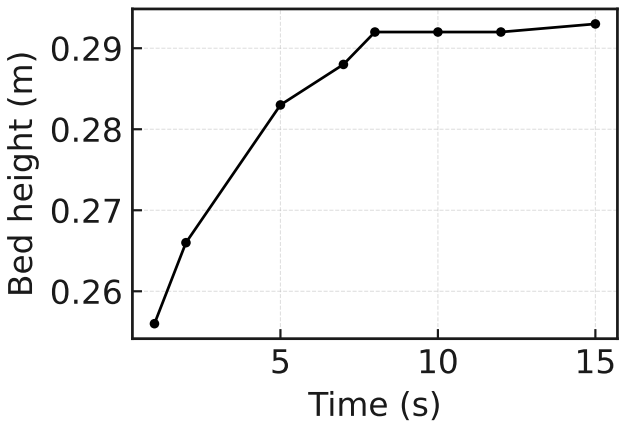

Figure 6: **Bed height $H(t)$ vs. time (Case 1).**

the experimental benchmark of $H_{\text{exp}} \approx 0.34\,\text{m}$ in Figure 7. All simulated cases under-predict the expansion height, with values in the range 0.28–$0.32\,\text{m}$. Among the model variations, the Syamlal–O'Brien drag model (along with Gidaspow viscosity)— Case 7—showed the best agreement, with $H_\infty \approx 0.32\,\text{m}$ ($\sim$6% error). The base case (Case 1) and other Gidaspow-based drag models predicted $H_\infty \approx 0.29$–$0.30\,\text{m}$. These results highlight that the *drag law* is the dominant factor in matching experimental bed expansion: models with voidage-dependent drag (Syamlal–O'Brien, Gidaspow) consistently outperform simpler closures. By contrast, changes in KTGF viscosity, conductivity, or pressure mainly affect the sharpness of the liquid–solid transition as will be seen later, but have limited impact on the bulk bed height.

D. Solids Volume Fraction

The axial distribution of the surface-averaged solids fraction was analyzed, with the surface averaging defined as: $\langle\alpha_s\rangle(z) = \big(1/A(z)\big)\int_{A(z)} \alpha_s(x,y)\,\mathrm{d}A$, obtained by area-weighted averaging on horizontal planes. Bed height was actually identified from the sharp drop in $\langle\alpha_s\rangle$. The z at which $\langle\alpha_s\rangle$ fell below a small threshold was chosen. Figure 8 shows representative profiles for three model sets (Cases 1, 7, 10). All cases exhibit a dense bottom region full of solids with slowly varying $\langle\alpha_s\rangle$, followed by a thin transition layer where $\mathrm{d}\langle\alpha_s\rangle/\mathrm{d}z$ peaks and the curve rapidly approaches zero. The thickness of the transition layer is governed by hydrodynamic dispersion (mixing caused by flow fluctuations) and by collisional/frictional stresses in the granular phase, both of which tend to smear solids upward. When these dispersive effects are weaker relative to interphase slip, the profile drops more abruptly, indicating a sharper liquid–solid interface. Conversely, stronger dispersion broadens the layer and yields a gentler decline in $\langle\alpha_s\rangle$ with height.

Case 7 (Syamlal–O'Brien drag) resulted in a bed height of $0.32\,\text{m}$, within 6% of the experiment. Case 1 (base) gave a height pf $0.29\,\text{m}$ and a slightly less diffuse transition, while Case 10 (Johnson–Jackson frictional stress) showed a broader transition layer, indicating stronger frictional compaction beneath a more gradually diluted top. These axial trends are consistent with the radial distributions reported later with Case 7 concentrating solids toward the core at a given elevation.

Radial profiles of the solids fraction $\alpha_s(r)$ were evaluated at two axial locations ($z = 0.27$ m, within the dense bed, and $z = 0.29$ m, near the liquid–solid interface; Fig. 9). These distributions complement the axial averages by highlighting lateral mixing and wall effects. In Case 1 (Fig. 9a), the profiles remain nearly flat across the radius at both heights, showing that toroidal circulation efficiently redistributes solids and yields a smooth, uniform interface with no wall channeling. Case 7 (Fig. 9b) exhibits a pronounced core–wall gradient, consistent with the Syamlal–O'Brien drag model that accentuates voidage dependence and concentrates solids near the axis. Case 10 (Fig. 9c) shows broader, more diffuse gradients. This leads to stronger fluctuations near the interface and a moderately higher bed expansion ($\sim$0.30 m), though still below Case 7. Overall, drag models with strong voidage dependence (e.g., Syamlal–O'Brien) sharpen the interface and favor core-dominated fluidization, whereas frictional stress models (e.g., Johnson–Jackson) broaden the transition region and amplify wall effects, reducing uniformity.

E. Velocity Field

The liquid-phase velocity field for Case 1 (Figure 10) is characterized by a strong upward core jet and near-wall downward recirculation that closes into a toroidal cell typical of fluidized beds. This core–upflow/wall–downflow structure suspends and disperses solids, while the side recirculation enhances mixing and mitigates channeling; the absence of large-scale oscillations or slugging indicates a stable fluidization regime.

The sparger holes were oriented *downwards* to limit blockage by coarse solids, causing the injected liquid to issue downward before turning upward. This generated local impingement and elevated shear in the lower bed, mobilizing particles that might otherwise remain trapped; the downward jets also fed the side currents, reinforcing the toroidal circulation and cross-sectional mixing, as noticeable in Figure 10.

Across KTGF and drag variations, the qualitative pattern persisted, with quantitative shifts in core-jet strength. Cases with greater bed expansion exhibited slightly stronger upward core velocities, consistent with the increased drag support required to suspend the solids.

The observed flow structures are highly relevant to the operational performance of fluidized-bed flotation systems. The strong upward core jet provides sustained suspension of coarse particles, increasing their residence time and likelihood of contacting rising bubbles. Simultaneously, the toroidal wall circulation promotes lateral mixing and minimizes stagnant zones, thereby enhancing bubble–particle collision frequency. The sharpness of the liquid–solid interface, governed by the chosen drag and KTGF closures, directly influences the selectivity of bubble–particle attachment and the degree of bubble carryover. A sharper interface corresponds to a more well-defined separation zone, reducing detachment caused by turbulent fluctuations. Thus, the nu-

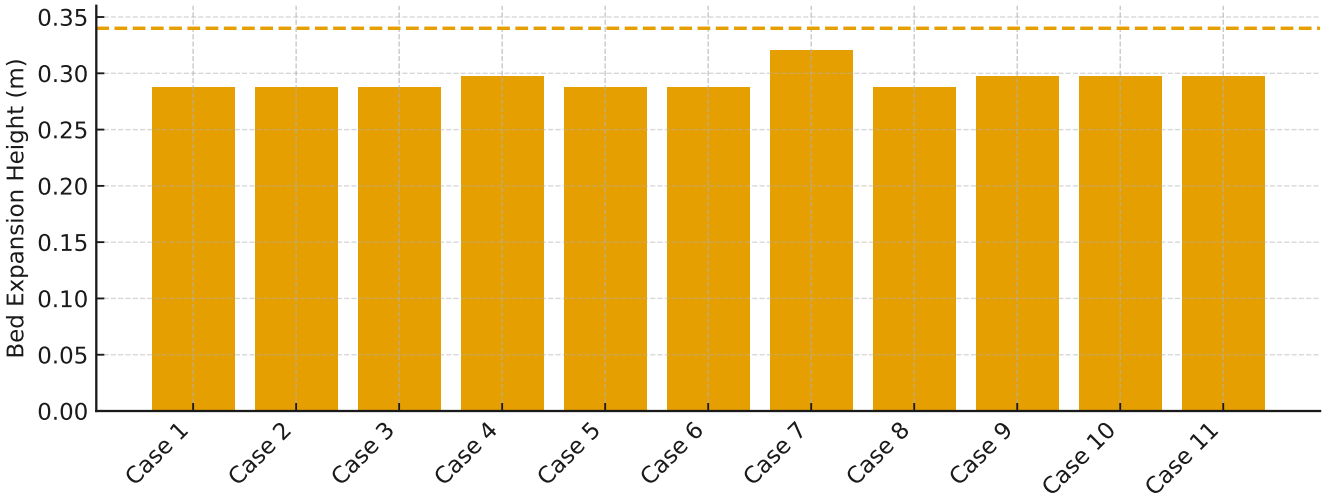

Figure 7: **Steady-state bed height for the eleven cases. Experimental bed height is included as the dashed line.**

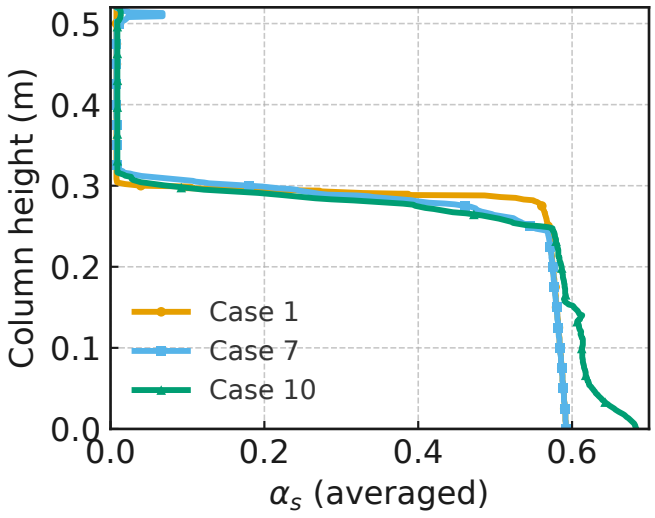

Figure 8: **Surface-averaged α_s vs. column height for Case 1 (base case), Case 7, and Case 10.**

merical flow patterns provide mechanistic insights into how hydrodynamics affects coarse-particle recovery efficiency in FBF systems.

IV. CONCLUSIONS

This study presented CFD simulations of liquid–solid fluidization in a scaled FBF cell using OpenFOAM's `twoPhaseEulerFoam` with eleven KTGF and drag model variations. Grid convergence was achieved at 650k cells, and predicted bed expansion heights (0.28–0.32 m) remained below the experimental value of 0.34 m.

The Syamlal–O'Brien drag closure gave the best agreement (∼0.32 m), confirming drag laws as the dominant factor, while KTGF variations mainly affected interface sharpness and radial solids distribution. The Johnson–Jackson frictional stress model produced broader gradients and stronger wall effects, whereas voidage-sensitive drag models sharpened the interface and concentrated solids near the core.

The model successfully reproduced steady-state flow structures such as the central jet and toroidal recirculation, validating the use of a two-fluid framework for this system. Overall, the results clarify the relative roles of drag and KTGF closures and provide guidance for extending CFD models toward reliable design and scale-up of FBF systems for coarse particle recovery. Future work will examine the sensitivity of bed expansion and flow structures to superficial velocity, as observed in experiments, and incorporate additional physics such as turbulent dispersion, lift, and added-mass effects, as well as particle polydispersity, to improve predictive capability.

ACKNOWLEDGEMENTS

The authors gratefully acknowledge the National Supercomputing Mission for providing access to computing resources on 'PARAM Himalaya' at IIT Mandi, supported by C-DAC, MeitY, and DST, Government of India. The authors also acknowledge Dr Angus Morrison and the Julius Kruttschnitt Mineral Research Centre (JKMRC), University of Queensland, for kindly providing the experimental data used in this study.

REFERENCES

[1] Carly Leonida. Flotation: The past, present and future of mineral processing? *Engineering and Mining Journal*, 222(6):60–65, 2021.

[2] K Demir, AJ Morrison, C Evans, J Kohmuench, and K Runge. The bubble size produced in a pilot HydroFloat® cell and its effects on flotation. *Minerals Engineering*, 218:109021, 2024.

[3] Graeme J Jameson. New directions in flotation machine design. *Minerals Engineering*, 23(11-13):835–841, 2010.

[4] Md Tariqul Islam and Anh V Nguyen. Parametric investigations of different variables on liquid–solid fluidization in a hydrofloat cell

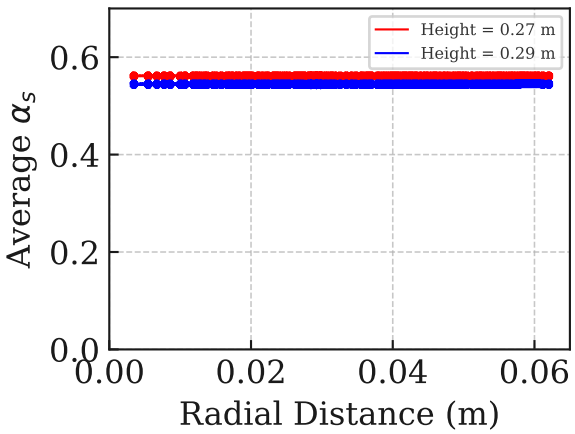

(a) **Case 1**

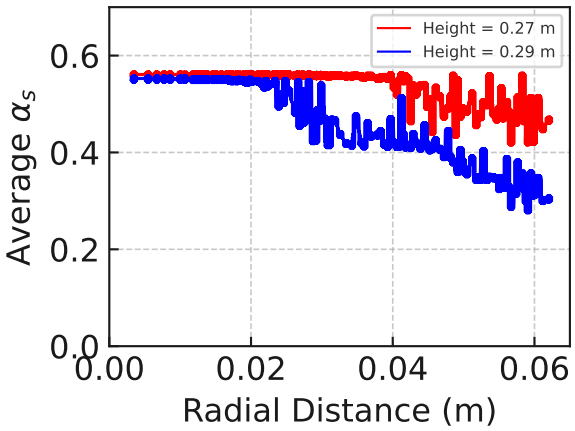

(b) **Case 7**

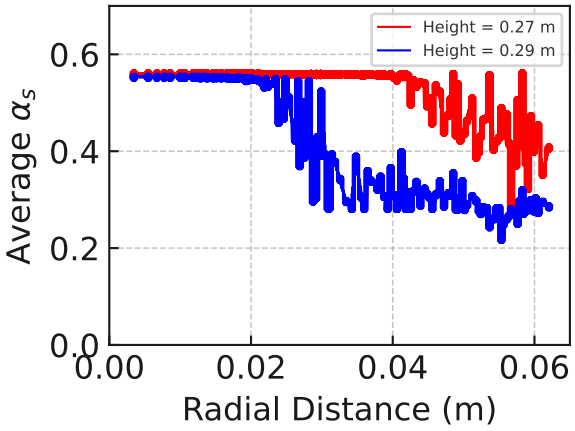

(c) **Case 10**

Figure 9: **Radial distribution of solids volume fraction α_s at two heights (0.27 m and 0.29 m) for Cases 1, 7, and 10.**

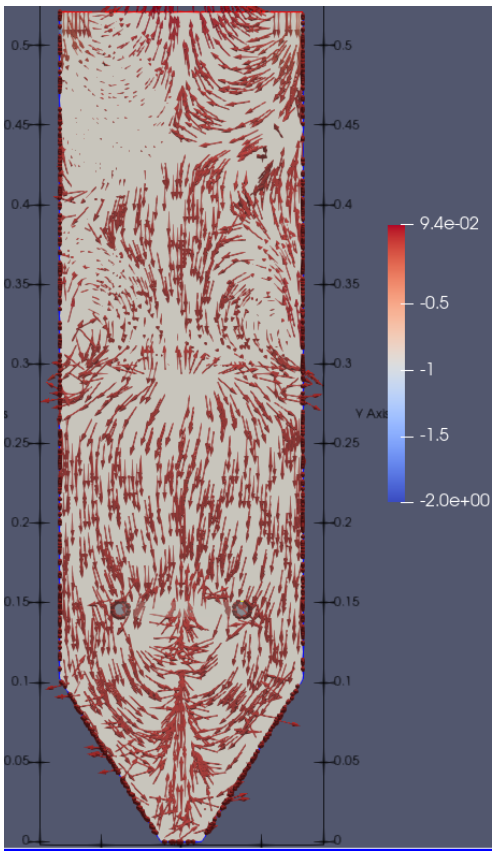

Figure 10: **Midplane liquid velocity vectors for Case 1.**

using computational fluid dynamics. *Chemical Engineering Research and Design*, 159:13–26, 2020.

[5] John D Anderson. *Computational fluid dynamics: the basics with applications*. McGraw-Hill New York, 2002.

[6] Ashish Raman. 3-D computational modelling of hindered-settling fluidised bed flotation cell having two phases. M.Tech. thesis, Indian Institute of Technology Mandi, May 2024.

[7] Dimitri Gidaspow. *Multiphase flow and fluidization: continuum and kinetic theory descriptions*. Academic Press, 1994.

[8] M Syamlal and TJ O'Brien. A generalized drag correlation for multiparticle systems. *Morgantown Energy Technology Center DOE Report*, 1987.

[9] Arpit Dwivedi. Computational modelling of multiphase flow in a fluidised bed flotation cell. M.S. thesis, Indian Institute of Technology Mandi, December 2022.

[10] Brian Edward Launder and Dudley Brian Spalding. The numerical computation of turbulent flows. In *Numerical prediction of flow, heat transfer, turbulence and combustion*, pages 96–116. Elsevier, 1983.

[11] Paul C Johnson and Roy Jackson. Frictional–collisional constitutive relations for granular materials, with application to plane shearing. *Journal of Fluid Mechanics*, 176:67–93, 1987.